nature photonics

Check for updates

OPEN
Single-cycle infrared waveform control

Philipp Steinleitner [1,6], Nathalie Nagl [1,2,6 ✉], Maciej Kowalczyk [1,2,3,6 ✉], Jinwei Zhang[1,4],
Vladimir Pervak[2], Christina Hofer [1,2,3], Arkadiusz Hudzikowski [5], Jarosław Sotor [5],
Alexander Weigel [1,3], Ferenc Krausz [1,2,3] and Ka Fai Mak [1 ✉]

Tailoring the electric-field waveform of ultrashort light pulses forms the basis for controlling nonlinear optical phenomena on their genuine, attosecond timescale. Here we extend waveform control from the visible and near-infrared—where it was previously demonstrated—to the mid-infrared spectral range. Our approach yields single-cycle infrared pulses over several octaves for the first time. Sub-10-fs pulses from a carrier-envelope-phase-stabilized, Kerr-lens-mode-locked, diode-pumped Cr:ZnS laser drive cascaded intrapulse difference-frequency generation and control the electric-field evolution of the resulting coherent emission over 0.9–12.0 μm. Sub-cycle field control in this wavelength range will be instrumental for launching and steering few-femtosecond electron/hole wavepackets in low-gap materials, extending the bandwidth of electronic signal processing to multi-terahertz frequencies, as well as for electric-field-resolved molecular fingerprinting of biological systems.

The confinement of laser light to a few periods of its oscillating electromagnetic fields gives rise to extreme nonlinear interactions—the control and exploitation of which requires precise control of the fields' temporal evolution[1]. Once this control became available[2], few-cycle-driven nonlinear optics permitted the reproducible generation of isolated attosecond pulses, in atomic gases[3] as well as in solids[4–6]. Optical-field control also opened the way to trigger solid-state electronic processes on a sub-femtosecond timescale[7–10] and, in combination with field-enhancing nanostructures[10–12], even with picojoule pulse energies[13].

Extreme nonlinear optics and its applications have predominantly been demonstrated in the near-infrared (near-IR) spectral region, where precision dispersion management over super-octave bandwidth and controlled few-cycle to single-cycle waveforms have become available[14]. Extension of waveform control to the mid-infrared (mid-IR) spectral range is motivated by a plethora of applications. Examples include the scaling of terahertz electronics[15–17] and orbital imaging and control[18,19] towards optical (≫1 THz) frequencies, the development of novel optoelectronic devices based on low-bandgap highly doped semiconductors[12,20] and the advancement of electric-field molecular fingerprinting of biological systems[21–23].

In the absence of suitable laser gain media, the frequency downconversion of femtosecond near-IR pulses has been used to produce coherent radiation in the mid-IR range spanning an octave or more[24–34], but full phase control over this vast bandwidth is lacking thus far. Adaptive optics have been demonstrated to shape mid-IR radiation over limited (sub-octave) bandwidth[35,36]. Scaling this approach to multi-octave spectral coverage would require the sub-division of the multi-octave spectral band into a number of channels, their independent modulation and subsequent interferometric recombination. These measures increase system complexity and impair the reproducibility of output waveforms[14]. Alternatively, the near-IR driver can be shaped before frequency conversion[37,38]. By using orientation-patterned nonlinear crystals, adiabatic difference-frequency generation has recently yielded super-octave

(1.8–4.4 μm) single-cycle mid-IR pulses with a pulse envelope that can be arbitrarily shaped[39]. None of these techniques have provided pulse-to-pulse reproducible waveforms so far.

In this Article, we present a new approach for coherent multi-octave mid-IR generation with an intrinsic capability of changing the relative phase of different spectral regions and thereby shaping the emerging waveform. Specifically, we create mid-IR waveforms in several spectral bands by cascaded intrapulse difference-frequency generation (IPDFG)[31,40] and manipulate their spectral phases by taking advantage of their different dependence characteristics on the carrier-envelope phase (CEP) of the driving pulse. The adjustment of the relative phase of different spectral components—across over 3.7 optical octaves—is achieved without the need for spatial separation and subsequent interferometric recombination[14]. Our approach yields the first multi-octave synthesis of single-cycle mid-IR waveforms, with a continuously adjustable, highly reproducible electric-field evolution. The concept is generalizable towards the synthesis of a wider variety of infrared waveforms by increasing the number of adjustable parameters, such as the control of spectral phase and amplitude of the driving pulse before the cascaded IPDFG.

Cascaded IPDFG

The basic principle of cascaded IPDFG is illustrated in Fig. 1, based on a simplified modelling of broadband light propagating through a nonlinear crystal (Supplementary Section 7). To isolate and visualize the relevant frequency-mixing processes, the driving laser is represented by two isolated narrowband spectral components (centred at 1.9 and 2.3 μm) of its entire spectrum, sharing the same CEP (Fig. 1, dashed black curves).

Difference-frequency mixing of the two driving components initially creates a peak at 30 THz. Since the two driving components share the same CEP value, the mixing product's CEP is invariant to CEP changes of the driver. This fundamental (zeroth order) IPDFG field, on further propagation in the nonlinear medium, mixes with one of the narrowband drivers to create components at 100 THz
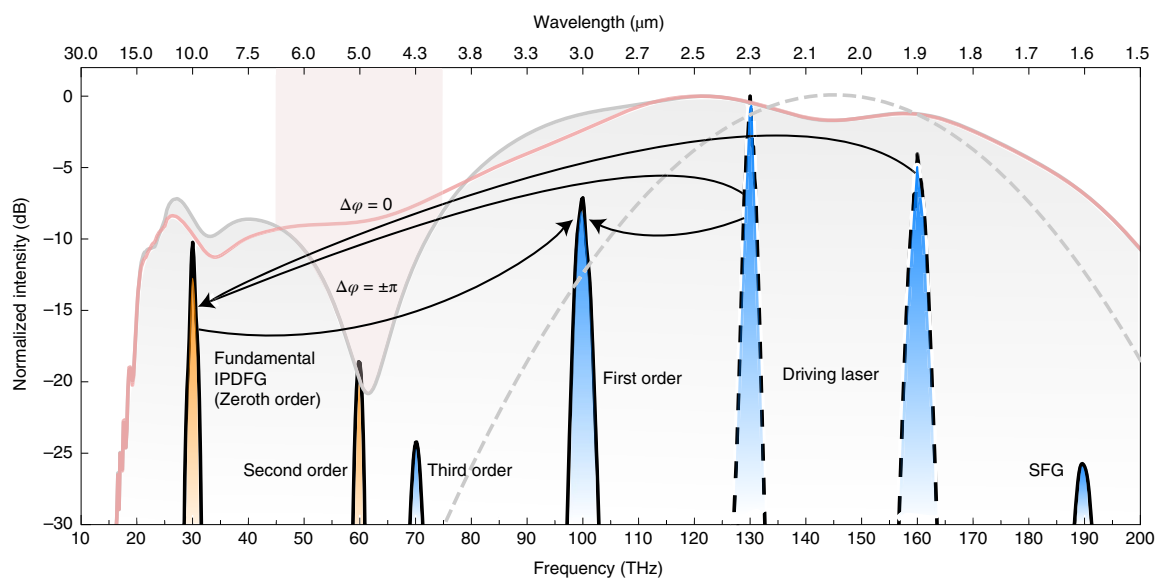
Fig. 1 | Waveform synthesis via cascaded nonlinear processes. Simulated mid-IR intensity spectrum generated in a 0.5-mm-thick ZGP crystal by two narrowband laser pulses centred at 130 THz (2.3 μm) and 160 THz (1.9 μm) (dashed black curves), simulated by using commercial nonlinear pulse propagation software. Downconverted radiation results from the difference-frequency mixing of differing orders (0–3). The most intense, fundamental component (zeroth order) is created by the mixing of the two narrowband inputs from the driving laser, whereas the higher orders (1–3) arise from further difference-frequency mixing of the preceding orders (0–2) with the driving laser. Further cascading does occur, but their progressively lower intensities mean that they play a negligible role in the dynamics. The CEP of the odd orders (shaded in blue) follow the changes in the CEP of the driving laser, whereas even orders are invariant (shaded in orange). By varying the CEP of the driving laser, the phase relation between the odd and even orders can be changed, resulting in a change in the total waveform. For a single driving pulse with a broad spectral width (simulated here with a spectral width of 44 THz and centred at 145 THz (dashed grey curve)), the pronounced spectral broadening of the different orders overlap to form a broad continuum (grey and light-red curves). In the region of the strongest overlap between odd and even mixing orders, at around 60 THz (light-red-shaded area), the interference between waveform components of differing CEP values leads to the modulation of spectral intensity with respect to the driving field's CEP. The red and grey curves depict the intensity distribution for the driving field's CEP set to yield constructive ($\Delta\varphi=0$) and destructive ($\Delta\varphi=\pm\pi$) interference, respectively. The same (second-order) susceptibility also implies sum-frequency generation (SFG) at about 190 THz, by mixing the 160 THz driver with the zeroth-order IPDFG band. This, however, is likely to be shrouded by the more efficient self-phase-modulation-induced spectral broadening of the driver in the ZGP crystal.

(first cascading order). This cascading effect continues with the re-mixing of the first order and one of the driving components to generate new frequencies near 60 THz (second order), which, in turn, generate the 70 THz band (third order)[40]. Depending on the cascading order, the CEP of the newly generated wavelength components will either be invariant to (even orders) or follow the changes in the CEP of the driver (odd orders). Consequently, any changes in the driver CEP modifies the combined electric-field waveform in the time domain. This also implies that the electric-field evolution of radiation emerging from cascaded nonlinear frequency mixing varies from pulse to pulse in the absence of CEP stabilization.

For a broadband driving pulse (Fig. 1, dashed grey curve), the fundamental and cascaded components merge into a continuum (Fig. 1, light-grey and light-red curves). Importantly, the spectral region where the even and odd orders overlap exhibit pronounced interference effects on tuning the CEP of the driving laser (Supplementary Section 6). Shifting the CEP by $\Delta\varphi=\pm\pi$ with respect to its reference that yielded the maximum mid-IR intensity (Fig. 1, light-red curve; $\Delta\varphi=0$) results in the maximum suppression of spectral intensity in this region by destructive interference (Fig. 1, light-grey curve). This change in the spectral distribution of mid-IR radiation underlines the necessity of CEP-stabilized driver light for reproducible multi-octave infrared waveform generation via cascaded second-order nonlinearities.

Single-cycle waveform-stabilized Cr:ZnS laser system
Frequency downconversion into the mid-IR spectral range can be most efficiently driven at the longest possible wavelengths[27–34]. This

also applies to the electro-optic sampling (EOS) of the generated mid-IR fields[32]. Mode-locked laser oscillators based on Cr-doped II–VI gain media offer ideal driver wavelengths for both purposes, but they have lacked CEP stability so far[30,41–43].

Here we demonstrate a CEP-stabilized femtosecond Cr:II–VI laser oscillator, with the Cr:ZnS active medium being directly pumped by laser diodes. Femtosecond pulses are generated by Kerr-lens mode locking, yielding 24 nJ pulses with a duration of 28 fs (full-width at half-maximum (FWHM)) at a repetition rate of approximately 23 MHz[44].

The output pulses undergo further spectral broadening via self-phase modulation (SPM) in a highly nonlinear bulk dielectric medium (Fig. 2a, TiO$_2$; Methods and Supplementary Section 2) to generate a spectrum spanning from 1.1 μm (272 THz) to 3.2 μm (94 THz) at the −20 dB level (Fig. 2b). Furthermore, despite the strong spectral broadening, the spatial intensity profile of the laser beam remains smooth and Gaussian-like (Fig. 2c, inset) with a laser-beam quality parameter $M^2 < 1.4$ (Supplementary Fig. 2). This value indicates excellent focusability for downstream experiments. The spectrally broadened pulses are temporally compressed in a set of specially designed chirped dielectric multilayer mirrors to a duration of 7.7 fs (FWHM; Fig. 2c), which is equivalent to one optical cycle at the spectral centroid position of 2.24 μm.

The spectrally broadened pulses are subsequently split with an uncoated wedged ZnS beam splitter. The two main reflections off the wedge's front (48 mW) and back (36 mW) surface are used as a gate pulse for characterizing the mid-IR waveform with EOS (Methods and Supplementary Section 5) and for carrier-envelope offset
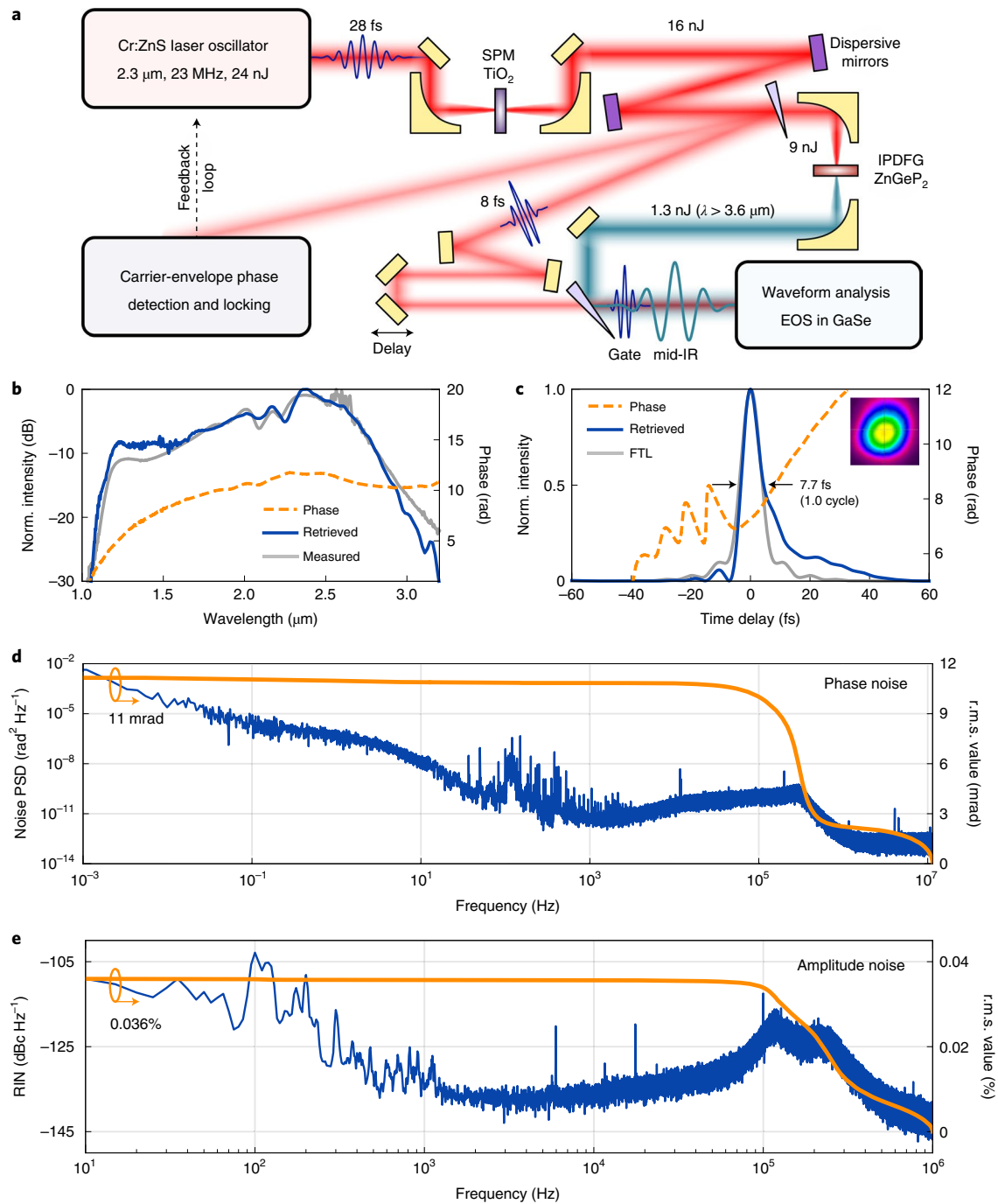
Fig. 2 | Experimental setup and characteristics of the single-cycle Cr:ZnS laser-based source. a, Front end of the experimental system is a home-built Kerr-lens-mode-locked CEP-stabilized Cr:ZnS oscillator delivering 28 fs pulses with a wavelength coverage between 1.9 and 2.7 μm (160 and 110 THz; at the −20 dB level) and a pulse energy of 24 nJ. The pulses are further spectrally broadened in a 0.5-mm-thick anti-reflection-coated TiO_2 plate via SPM. The output of the broadening stage (16 nJ) is temporally compressed by chirped multilayer mirrors and split into three branches using a ZnS wedge. The first reflection is used as a gate pulse for EOS in a 0.1-mm-thick GaSe crystal ($\theta = 35°$, $\varphi = 30°$). The second reflection is used for f_{ceo} detection and stabilization. The transmitted beam (9 nJ) is used for mid-IR generation in a 1-mm-thick ZGP crystal ($\theta = 51°$, $\varphi = 0°$). To characterize the generated mid-IR pulses (cyan waveform), they are combined with the gate pulse (blue waveform) using a second ZnS wedge for EOS. **b**, Measured intensity spectrum after the broadening stage (grey curve) compared with the retrieved spectrum (blue curve) from a second-harmonic frequency-resolved optical gating (SHG-FROG) measurement. The corresponding spectral phase is shown in orange. **c**, Temporal intensity profile (blue curve) and temporal phase (orange curve) of the compressed pulse as retrieved from the SHG-FROG measurement, together with the Fourier-transform limit (FTL) of the measured intensity spectrum (grey curve). The inset shows a spatial beam profile of the broadband pulses, with $M^2 < 1.4$. **d**, CEP noise power spectral density (PSD) of the 7.7- fs pulses (blue curve) and the corresponding r.m.s. phase noise integrated between 0.001 Hz and 11.43 MHz (orange curve). **e**, Relative intensity noise (RIN) of the 7.7 fs pulses (blue curve) and the corresponding r.m.s. noise integrated between 10 Hz and 1 MHz (orange curve). The frequency span differs from the one in **d** due to limitations of the employed measurement device.
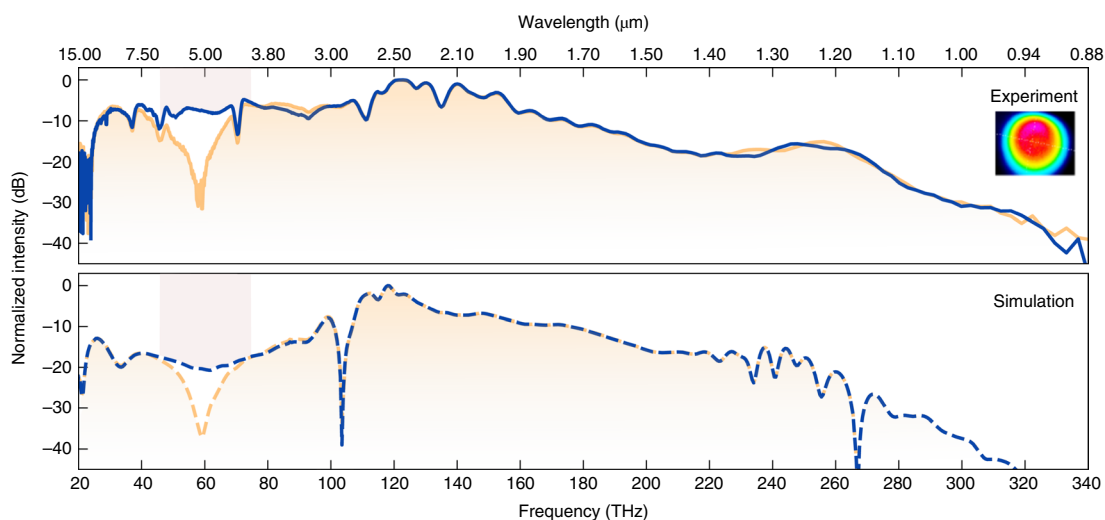
Fig. 3 | Infrared supercontinuum from cascaded IPDFG. Blue curves show the measured (solid) and simulated (dashed) spectra of the *p*-polarized IPDFG stage output for a relative phase of $\Delta\varphi = 0$ (constructive interference). The orange curves show the same settings as the blue curves, but for a relative phase of $\Delta\varphi = \pi$ (destructive interference). The light-red-shaded area shows the overlap region where interference effects occur (Fig. 1). The inset shows the spatial beam profile of the mid-IR continuum ($\lambda > 3.6\,\mu m$, $\Delta\varphi = 0$). The sharp features showing up near 100 and 270 THz in the simulations (both $\Delta\varphi = 0$ and $\Delta\varphi = \pi$) are probably artefacts arising from numerical approximations. The spectral resolution of 50 nm—chosen for higher signal-to-noise ratios—was insufficient to verify their presence.

frequency (f_{ceo}) detection, respectively. The f_{ceo} beat note is detected in an *f*–*2f* interferometer with a 60 dB signal-to-noise ratio (100 kHz resolution bandwidth) and locked to zero via pump-power modulation[45]. This results in a CEP identical for each laser pulse and continuously tunable by adjusting the feedback loop—a crucial feature for the controlled shaping of mid-IR waveforms generated by cascaded frequency-mixing processes. The CEP noise, measured at the output of the broadening stage (out of the feedback control loop), exhibits a root mean square (r.m.s.) jitter of 11 mrad integrated from 0.001 Hz up to the Nyquist frequency of 11.43 MHz (Fig. 2d, Methods and Supplementary Section 3). This represents one of the highest CEP stabilities ever reported[46,47], owing, among others, to the high amplitude stability of the diode-pumped Cr:ZnS laser driver, which yields an integrated relative intensity noise of 0.036% (r.m.s. value, measured between 10 Hz and 1 MHz) after the broadening stage (Fig. 2e). The outstanding stability of the single-cycle near-IR waveforms indicated by these noise figures is the key prerequisite for highly reproducible mid-IR waveform generation.

Controlled single-cycle waveforms in the mid-IR region

The beam traversing the ZnS wedge (Fig. 2a), with an average power of 215 mW, is focused into a 1-mm-thick ZnGeP$_2$ (ZGP) crystal for frequency downconversion via cascaded IPDFG (Methods and Supplementary Section 4). The radiation exiting the nonlinear crystal consists of the field of the transmitted driver pulse as well as the field resulting from the frequency-mixing processes (Fig. 1). The driver field has two orthogonal components of equal magnitude (Methods), one perpendicular and one parallel to the linearly polarized products of the frequency-mixing processes. As a consequence, the mid-IR components originating from IPDFG and the driver components with the same polarization together result in a coherent near-IR-to-mid-IR supercontinuum. Its spectrum was characterized, behind a polarizer, using a monochromator with multiple gratings and a pyroelectric detector (Fig. 3). The generated infrared supercontinuum (Fig. 3, top) spans from 25 THz (12.0 µm) to 330 THz (0.9 µm) at the −30 dB level, equivalent to over 3.7 octaves, limited at both ends by the transmission window of ZGP. This agrees well with our simulations based on the experimental parameters (Fig. 3, bottom).

By locking the CEP of the laser to a value ensuring constructive interference ($\Delta\varphi = 0$) between the cascading orders of the IPDFG process, we maximized the spectral intensity in the region of spectral overlap between the odd and even cascading orders (Fig. 1) from 45 THz (6.7 µm) to about 75 THz (4.0 µm) (Fig. 3, blue solid curve). On changing the CEP of the driver pulse with respect to the (unknown) reference that yielded the maximum mid-IR intensity by $\Delta\varphi = \pi$, a pronounced dip developed in the overlap region (Fig. 3, orange solid line) due to destructive interference. This effect is also verified by numerical simulations (Fig. 3, bottom). With the beam path purged with nitrogen to reduce ambient absorption, the power of the mid-IR part of the supercontinuum ($\lambda > 3.6\,\mu m$, $\Delta\varphi = 0$) is 31 mW (1.3 nJ; Fig. 2a), corresponding to an optical-to-optical conversion efficiency of 14% for the IPDFG process. Furthermore, the corresponding spatial beam profile (Fig. 3, inset) exhibits an excellent mid-IR beam quality.

EOS[48] has recently been advanced to optical frequencies of several hundred terahertz[49], and hence, it is ideally suited for the direct measurement of electric-field waveforms[15,17–19,50,51]. Using part of the 7.7 fs laser pulses (Fig. 2c) as the gate pulse, we electro-optically sampled the mid-IR part of the supercontinuum generated by cascaded IPDFG in a 0.1-mm-thick GaSe crystal (Methods and Supplementary Fig. 3). The EOS trace—indicative of the actual electric waveform[51]—exhibits a clean cosine-pulse-like temporal profile for $\Delta\varphi = 0$ (Fig. 4a, blue curve). The main peak coincides with the central peak of the calculated intensity envelope (Fig. 4b, blue curve) and indicates an FWHM pulse duration of 20 fs—equivalent to 0.9 optical cycles at the spectral centroid of 6.6 µm. The full supercontinuum exiting the nonlinear crystal, as measured by the monochromator (Fig. 3), can support even shorter pulses. If needed, appropriate spectral filters will be used to separate and isolate the controllable mid-IR waveforms from their driving fields for spectroscopic applications. Figure 4c (blue curve) shows the spectral intensity obtained by Fourier transforming the measured EOS trace. The resulting spectrum is, as expected, narrower than that measured using a monochromator (Fig. 3), given the EOS detection limit of approximately 100 THz for a gate-pulse duration of 7.7 fs (Fig. 2c).

Most interestingly, the EOS trace can be continuously changed (Fig. 4a) by tuning the relative phase $\Delta\varphi$ from 0 to π. The trace is transformed from a clean cosine-pulse-like temporal profile ($\Delta\varphi = 0$)
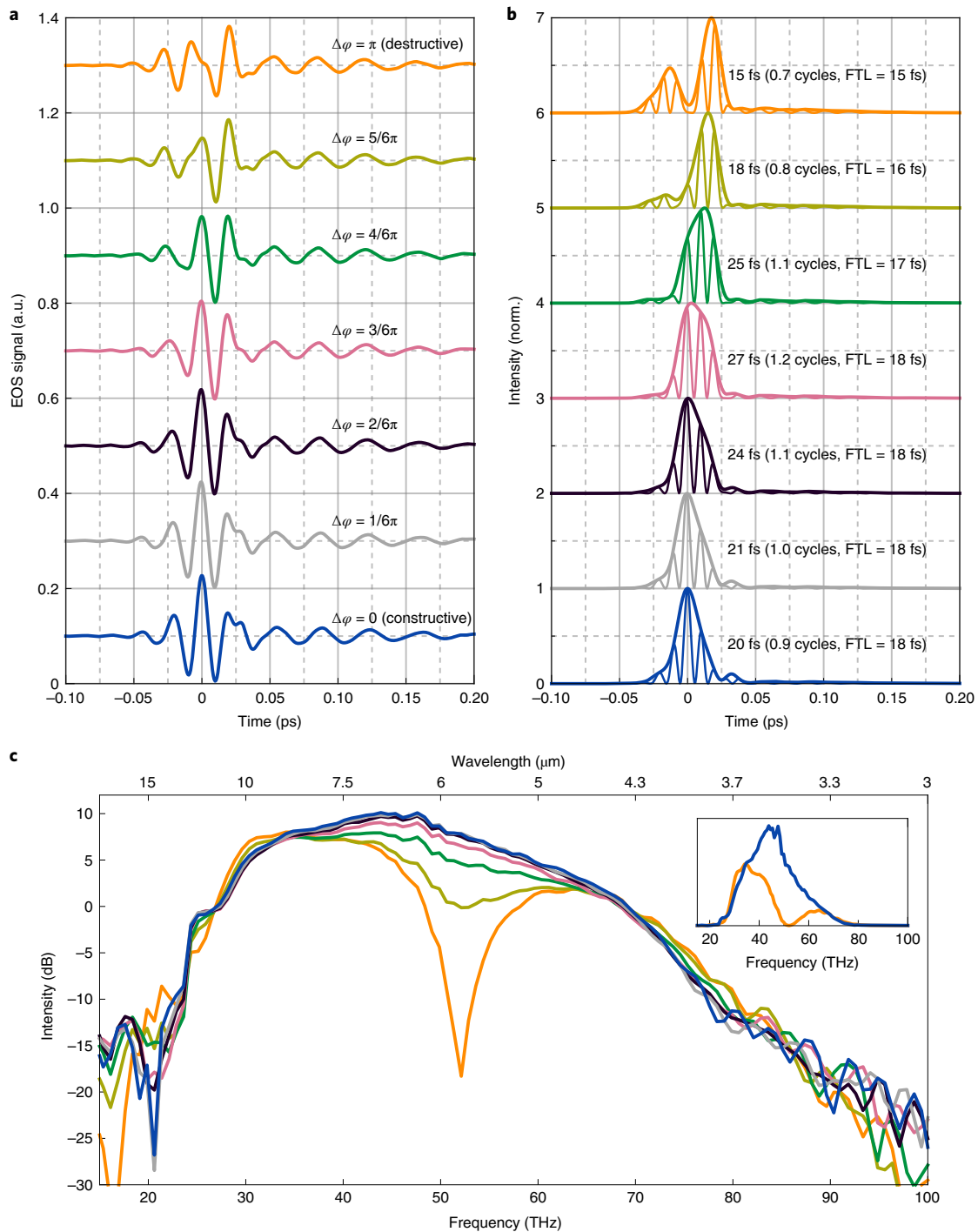
Fig. 4 | Monolithic-waveform synthesis in the mid-IR range. a, EOS time-domain data for different relative phases $\Delta\varphi$. Constructive interference occurs for a value of 0, whereas the strong modification of the mid-IR waveform for π indicates destructive interference. **b**, Corresponding intensity envelopes, extracted FWHM pulse durations, number of optical cycles calculated for the spectral centroid and FTL based on the derived spectral intensities. **c**, Corresponding spectral intensities for different relative phases, as extracted via the Fourier transformation of the time-domain data. Constructive interference occurs for $\Delta\varphi = 0$, whereas the strong spectral dip for $\Delta\varphi = \pi$ indicates destructive interference between the spectrally overlapping components originating from even and odd IPDFG orders. The inset shows the extreme spectra (constructive and destructive) on a linear scale.

to a sine-like profile ($\Delta\varphi = 3/6\pi$) and then to a double-pulsed structure ($\Delta\varphi = \pi$). The evaluation of the intensity envelopes (Fig. 4b) shows that all the measured pulses are temporally well compressed, featuring single to sub-cycle pulse durations. The corresponding spectra (Fig. 4c) exhibit similar spectral characteristics as observed using a monochromator (Fig. 3), however with a dip appearing to

be slightly shifted in frequency by 5 THz. This is likely caused by additional nonlinear mixing of the supercontinuum ($\lambda < 3\,\mu m$) with the gate pulse in the GaSe detection crystal. Nevertheless, this process is CEP invariant, and the observed changes in the EOS traces for different $\Delta\varphi$ values (Fig. 4a) are reproduced by simulations (Supplementary Fig. 4).

Conclusions and outlook

We have reported broadband waveform manipulation in the mid-IR spectral range. Cascaded difference-frequency mixing in a single nonlinear crystal enables waveform adjustment across multiple octaves, without the need for the spatial separation of spectral bands. This monolithic approach to waveform manipulation eliminates instabilities originating from beam-pointing fluctuations and timing jitter inherent in multiple-channel schemes for multi-octave synthesis[14]. With the control parameter being the CEP of the driver laser pulse, no additional dispersive material is required in the mid-IR beam path to manipulate the waveform. As a result, temporal confinement close to a single-field cycle can be preserved for different waveforms without demanding multi-octave dispersion management. For these reasons, the generated waveforms are inherently robust, with their reproducibility solely depending on that of the driver waveform.

The fidelity of the reported mid-IR waveforms benefits from the unprecedented CEP and amplitude stability and the resultant reproducibility of single-cycle waveforms of our diode-pumped Cr:ZnS oscillator-based source. The 1.7 MW peak power of these waveforms can be boosted beyond the 10 MW level without substantial added noise by diode-pumped Cr:ZnS amplifiers[52]. The higher peak intensity allows the use of nonlinear crystals with lower nonlinear coefficients but broader window of transparency for extending the mid-IR continuum towards the low-terahertz regime[34]. It also extends the SPM-generated near-IR continuum towards the visible, yielding few-femtosecond pulses for EOS of the entire 300 THz infrared supercontinuum demonstrated[49].

These advances offer technical capabilities unavailable to date. They include the temporal confinement of coherent multi-octave infrared light to sub-cycle transients of several femtosecond duration and—by introducing more control parameters (for example, via spectral manipulation of the driver waveform)—the sculpting of waveforms with sub-femtosecond-scale precision. Multi-octave infrared-field synthesis can probably impact research at several frontiers, including the advancement of electronic signal processing[7–10] and electric-field-resolved molecular fingerprinting of biological systems[23].

Online content

Any methods, additional references, Nature Research reporting summaries, source data, extended data, supplementary information, acknowledgements, peer review information; details of author contributions and competing interests; and statements of data and code availability are available at https://doi.org/10.1038/s41566-022-01001-2.

References

1. Brabec, T. & Krausz, F. Intense few-cycle laser fields: frontiers of nonlinear optics. *Rev. Mod. Phys.* **72**, 545–591 (2000).
2. Baltuška, A. et al. Attosecond control of electronic processes by intense light fields. *Nature* **421**, 611–615 (2003).
3. Kienberger, R. et al. Atomic transient recorder. *Nature* **427**, 817–821 (2004).
4. Luu, T. T. et al. Extreme ultraviolet high-harmonic spectroscopy of solids. *Nature* **521**, 498–502 (2015).
5. Langer, F. et al. Symmetry-controlled temporal structure of high-harmonic carrier fields from a bulk crystal. *Nat. Photon.* **11**, 227–231 (2017).
6. Ghimire, S. & Reis, D. A. High-harmonic generation from solids. *Nat. Phys.* **15**, 10–16 (2019).
7. Schiffrin, A. et al. Optical-field-induced current in dielectrics. *Nature* **493**, 70–74 (2013).
8. Higuchi, T., Heide, C., Ullmann, K., Weber, H. B. & Hommelhoff, P. Light-field-driven currents in graphene. *Nature* **550**, 224–228 (2017).
9. Vampa, G. et al. Strong-field optoelectronics in solids. *Nat. Photon.* **12**, 465–468 (2018).
10. Rybka, T. et al. Sub-cycle optical phase control of nanotunnelling in the single-electron regime. *Nat. Photon.* **10**, 667–670 (2016).
11. Ludwig, M. et al. Sub-femtosecond electron transport in a nanoscale gap. *Nat. Phys.* **16**, 341–345 (2020).
12. Dombi, P. et al. Strong-field nano-optics. *Rev. Mod. Phys.* **92**, 025003 (2020).
13. Hanus, V. et al. Light-field-driven current control in solids with pJ-level laser pulses at 80 MHz repetition rate. *Optica* **8**, 570–576 (2021).
14. Manzoni, C. et al. Coherent pulse synthesis: towards sub-cycle optical waveforms. *Laser Photonics Rev.* **9**, 129–171 (2015).
15. Langer, F. et al. Lightwave-driven quasiparticle collisions on a subcycle timescale. *Nature* **533**, 225–229 (2016).
16. Reimann, J. et al. Subcycle observation of lightwave-driven Dirac currents in a topological surface band. *Nature* **562**, 396–400 (2018).
17. Langer, F. et al. Lightwave valleytronics in a monolayer of tungsten diselenide. *Nature* **557**, 76–80 (2018).
18. Cocker, T. L., Peller, D., Yu, P., Repp, J. & Huber, R. Tracking the ultrafast motion of a single molecule by femtosecond orbital imaging. *Nature* **539**, 263–267 (2016).
19. Peller, D. et al. Sub-cycle atomic-scale forces coherently control a single-molecule switch. *Nature* **585**, 58–62 (2020).
20. Fischer, M. P. et al. Field-resolved detection of the temporal response of a single plasmonic antenna in the mid-infrared. *Optica* **8**, 898–903 (2021).
21. Coddington, I., Swann, W. C. & Newbury, N. R. Time-domain spectroscopy of molecular free-induction decay in the infrared. *Opt. Lett.* **35**, 1395–1397 (2010).
22. Kowligy, A. S. et al. Infrared electric field sampled frequency comb spectroscopy. *Sci. Adv.* **5**, eaaw8794 (2019).
23. Pupeza, I. et al. Field-resolved infrared spectroscopy of biological systems. *Nature* **577**, 52–59 (2020).
24. Junginger, F. et al. Single-cycle multiterahertz transients with peak fields above 10 MV/cm. *Opt. Lett.* **35**, 2645–2647 (2010).
25. Fuji, T. & Nomura, Y. Generation of phase-stable sub-cycle mid-infrared pulses from filamentation in nitrogen. *Appl. Sci.* **3**, 122–138 (2013).
26. Liang, H. et al. High-energy mid-infrared sub-cycle pulse synthesis from a parametric amplifier. *Nat. Commun.* **8**, 141 (2017).
27. Zhang, J. et al. Multi-mW, few-cycle mid-infrared continuum spanning from 500 to 2250 cm⁻¹. *Light Sci. Appl.* **7**, 17180 (2018).
28. Gaida, C. et al. Watt-scale super-octave mid-infrared intrapulse difference frequency generation. *Light Sci. Appl.* **7**, 94 (2018).
29. Novák, O. et al. Femtosecond 8.5 μm source based on intrapulse difference-frequency generation of 2.1 μm pulses. *Opt. Lett.* **43**, 1335–1338 (2018).
30. Vasilyev, S. et al. Super-octave longwave mid-infrared coherent transients produced by optical rectification of few-cycle 2.5-μm pulses. *Optica* **6**, 111–114 (2019).
31. Wang, Q. et al. Broadband mid-infrared coverage (2–17 μm) with few-cycle pulses via cascaded parametric processes. *Opt. Lett.* **44**, 2566–2569 (2019).
32. Butler, T. P. et al. Multi-octave spanning, Watt-level ultrafast mid-infrared source. *J. Phys. Photonics* **1**, 044006 (2019).
33. Lesko, D. M. B. et al. A six-octave optical frequency comb from a scalable few-cycle erbium fibre laser. *Nat. Photon.* **15**, 281–286 (2021).
34. Elu, U. et al. Seven-octave high-brightness and carrier-envelope-phase-stable light source. *Nat. Photon.* **15**, 277–280 (2021).
35. Cartella, A. et al. Pulse shaping in the mid-infrared by a deformable mirror. *Opt. Lett.* **39**, 1485–1488 (2014).
36. Jakob, M. A. et al. Generation and characterization of tailored MIR waveforms for steering molecular dynamics. *Opt. Express* **27**, 26979–26988 (2019).
37. Eickemeyer, F., Kaindl, R. A., Woerner, M., Elsaesser, T. & Weiner, A. M. Controlled shaping of ultrafast electric field transients in the mid-infrared spectral range. *Opt. Lett.* **25**, 1472–1474 (2000).
38. Witte, T., Kompa, K. L. & Motzkus, M. Femtosecond pulse shaping in the mid infrared by difference-frequency mixing. *Appl. Phys. B* **76**, 467–471 (2003).
39. Krogen, P. et al. Generation and multi-octave shaping of mid-infrared intense single-cycle pulses. *Nat. Photon.* **11**, 222–226 (2017).
40. Kessel, A. et al. Generation of multi-octave spanning high-energy pulses by cascaded nonlinear processes in BBO. *Opt. Express* **24**, 5628–5637 (2016).
41. Mirov, S. B. et al. Frontiers of mid-IR lasers based on transition metal doped chalcogenides. *IEEE J. Sel. Topics Quantum Electron.* **24**, 1–29 (2018).
42. Vasilyev, S. et al. Middle-IR frequency comb based on Cr:ZnS laser. *Opt. Express* **27**, 35079–35087 (2019).
43. Nagl, N. et al. Directly diode-pumped, Kerr-lens mode-locked, few-cycle Cr:ZnSe oscillator. *Opt. Express* **27**, 24445–24454 (2019).
44. Nagl, N., Pervak, V., Krausz, F. & Mak, K. F. Milliwatt-level multi-octave mid-infrared generation by a diode-pumped Cr:ZnS oscillator. In *2021 Conference on Lasers and Electro-Optics Europe and European Quantum Electronics Conference* cf_6_1 (Optica Publishing Group, 2021).
45. Okubo, S., Onae, A., Nakamura, K., Udem, T. & Inaba, H. Offset-free optical frequency comb self-referencing with an *f*-2*f* interferometer. *Optica* **5**, 188–192 (2018).

46. Liao, R. et al. Active *f*-to-2*f* interferometer for record-low jitter carrier-envelope phase locking. *Opt. Lett.* **44**, 1060–1063 (2019).

47. Lemons, R. et al. Carrier-envelope phase stabilization of an Er:Yb:glass laser via a feed-forward technique. *Opt. Lett.* **44**, 5610–5613 (2019).

48. Wu, Q. & Zhang, X.-C. Free-space electro-optics sampling of mid-infrared pulses. *Appl. Phys. Lett.* **71**, 1285–1286 (1997).

49. Keiber, S. et al. Electro-optic sampling of near-infrared waveforms. *Nat. Photon.* **10**, 159–162 (2016).

50. Riek, C. et al. Direct sampling of electric-field vacuum fluctuations. *Science* **350**, 420–423 (2015).

51. Sulzer, P. et al. Determination of the electric field and its Hilbert transform in femtosecond electro-optic sampling. *Phys. Rev. A* **101**, 033821 (2020).

52. Qu, S. et al. 1.5-W diode-pumped femtosecond Cr:ZnS amplifier. In *2021 Conference on Lasers and Electro-Optics Europe and European Quantum Electronics Conference* 1 (IEEE, 2021).

Methods

CEP locking. The detection of f_{ceo} was performed in a common-path f–$2f$ interferometer around 1,230 nm with a periodically poled lithium niobate crystal serving as a nonlinear medium for second-harmonic generation. For CEP stabilization (that is, setting $f_{ceo} = 0$), we adopted a self-referenced locking concept[45] combined with an active phase control realized via current modulation of the laser pump diode. An additional CaF_2 wedge pair was implemented at the input of the interferometer, enabling to set the arbitrary operation point of the locking loop and hence tune the CEP on demand within the full phase range without introducing any chirp in the mid-IR waveform. The out-of-loop CEP stability was investigated in a second f–$2f$ interferometer with the gate beam as the input.

Nonlinear crystals. For nonlinear spectral broadening, the output of the laser oscillator is tightly focused ($\varnothing = 20 \mu m$) into a 0.5-mm-thick bulk rutile (TiO_2) plate to induce SPM. To enhance transmission through TiO_2 and suppress birefringent effects, the plate was coated with an anti-reflection material for the spectral range of 1.2–3.2 μm and cut in the (001) orientation to be used at normal incidence.

In the IPDFG stage, a 1-mm-thick ZGP crystal is used in the type I phase-matching configuration ($\theta = 51°$, $\varphi = 0°$). To achieve this, a half-wave plate is needed to rotate the polarization of the driving pulses to feature two orthogonal field components of equal magnitude. A peak intensity of 150 GW cm^{-2} allows for an efficient nonlinear conversion into the mid-IR spectral region.

Waveform characterization. To trace the changes in the mid-IR waveform caused by the change in the CEP of the driving laser, the method of EOS[48,53] is utilized under a nitrogen-purged environment. The gate beam and mid-IR beam are combined using a ZnS wedge (Fig. 2a). Subsequently, they are focused into a 0.1-mm-thick GaSe detection crystal, where we employ type I phase matching ($\varphi = 30°$) at an external angle of $\theta = 35°$. Therefore, the sum frequency of the two pulses is generated, resulting in an effective polarization rotation of the gate pulse, which is proportional to the electric field of the mid-IR range. This polarization rotation is analysed with an ellipsometer comprising a quarter-wave plate, a Wollaston prism and a balanced detection scheme. By varying the time delay between the gate and mid-IR pulses using an electronic stage, we can obtain a trace indicative of the mid-IR waveform.

Data availability

The datasets generated during and/or analysed in this study are available from the corresponding authors upon reasonable request.

Code availability

The codes that support this study are available from the corresponding authors upon reasonable request.

References

53. Hofer, C. et al. Quantum-efficiency and bandwidth optimized electro-optic sampling. In *2019 Conference on Lasers and Electro-Optics Europe European Quantum Electronics Conference (CLEO/Europe-EQEC)* cf_p_15 (Optica Publishing Group, 2019).

Author contributions

The research was initiated by F.K. and led by K.F.M. F.K., K.F.M., P.S., N.N. and M.K. planned and designed the study, with contributions from A.W. and J.Z. P.S., N.N. and M.K. performed the experiments and analysed the data, with contributions from C.H. and A.W. V.P. developed the dispersive multilayer mirrors. A.H. and J.S. developed a low-noise laser diode driver for CEP locking. K.F.M., F.K., P.S., N.N. and M.K. wrote the manuscript. All the authors read and finalized the manuscript.

Funding

Competing interests

Additional information